

# Isotropic single-objective microscopy: theory and experiment

Eric Le Moal, Emeric Mudry, Patrick C. Chaumet, Patrick Ferrand, and Anne Sentenac\*

*Institut Fresnel, CNRS, Aix-Marseille Université, Ecole Centrale Marseille,  
Campus de St Jérôme, 13013 Marseille, France*

*\*Corresponding author: anne.sentenac@fresnel.fr*

Received March 25, 2011; revised May 31, 2011; accepted June 1, 2011;  
posted June 10, 2011 (Doc. ID 144816); published July 11, 2011

Isotropic single-objective (ISO) microscopy is a recently proposed imaging technique that can theoretically exhibit the same axial and transverse resolutions as 4Pi microscopy while using a classical single-objective confocal microscope. This achievement is obtained by placing the sample on a mirror and shaping the illumination beam so that the interference of the incident and mirror-reflected fields yields a quasi-spherical spot. In this work, we model the image formation in the ISO fluorescence microscope and simulate its point spread function. Then, we describe the experimental implementation and discuss its practical difficulties. © 2011 Optical Society of America

OCIS codes: 180.1790, 180.2520, 180.6900.

## 1. INTRODUCTION

Sharp focusing of light beams is the keystone of numerous applications in crucial technological fields, including far-field optical microscopy [1], optical writing and reading for high-density data storage [2,3], and trapping and manipulation of nanoparticles [4–6]. Objective lenses of high numerical aperture with high-order aberration corrections have been developed to reduce the dimensions of the focal spot down to the diffraction limit. Still, optical focusing systems based on a single-lens geometry cannot focus light into ideally spherical volumes because the illumination comes only from one side of the focal point. As a result, the focal spot is elongated along the lens optical axis, with an axial dimension about threefold larger than the transverse ones, at best. Such a pronounced anisotropy constitutes a serious drawback for any three-dimensional (3D) application in the above-mentioned fields of technology. This fundamental issue has motivated the study of many different approaches, among which are, notably, the use of pupil filters to control the amplitude and/or the phase distribution of the input field [7–11] and (or together with) the use of peculiar polarization modes [12–14]. These approaches allow engineering, to a certain extent, the spatial field distribution at the focus; however, they bring about only modest improvement concerning the axial dimension of the focal spot [15].

In the specific field of 3D fluorescence imaging in biology, the resolution issue has been addressed through sophisticated approaches relying on nonlinear excitation processes and optical focusing systems based on a multiple-lens geometry [16,17]. In 4Pi microscopy, the sample is sandwiched between two opposing lenses having the same optical axes and front focal planes. Focusing light through both lenses in a coherent way yields an interference pattern that exhibits a quasi-spherical intensity peak surrounded by some sidelobes [18–20]. The 4Pi focusing (and detection) scheme has brought about a spectacular improvement in the axial resolution of 3D

fluorescence imaging [21–23] but it requires a careful alignment of the lenses and turns out to be quite sensitive to mechanical drifts.

Inspired by a work on mirror-assisted optical diffraction tomography with isotropic resolution [24], we recently demonstrated the principle of an isotropic single-objective (ISO) focusing scheme in which light can be focused into a quasi-spherical spot thanks to one microscope objective lens, a mirror, and a specially shaped incident beam [25]. In a simplified view, the ISO focusing setup is equivalent to the 4Pi setup in which the role of the second lens is played by the image of the first one in a mirror.

In this paper, we detail the concept of ISO microscopy and describe the numerical technique that permits us to simulate with the least approximations possible the point spread function (PSF) of a realistic ISO fluorescence microscope. Then, we show how an ISO fluorescence microscope can be built out of a conventional confocal microscope and display experimental PSFs. We point out the main features that can hamper the performances of the microscope and give some hints to overcome them.

## 2. PRINCIPLES OF ISO FOCUSING AND SIMULATIONS

The principles of ISO focusing were described in [25]. Here we recall its main idea for completeness and detail the simulation technique.

### A. Time-Reversal Focusing Theory

To focus light into a spherical spot, the illumination should ideally reach the focal point from every possible direction. To approach this spherical illumination with a single-objective lens, we place a mirror near the focal plane and engineer the incident wavefront so that part of the incident and mirror-reflected fields converge toward the focal point.

Hereafter, the sample space (after the objective lens) is described by a Cartesian set of coordinates  $(x, y, z)$  with the origin placed at the focal point of the lens and the  $z$  axis corresponding to its optical axis. In this part, for simplicity, the mirror plane is set at the  $z = 0$  plane, which corresponds to the focal plane. To describe the incident beam, it is convenient to introduce the polar and azimuthal angles  $(\theta, \phi)$  associated to the unit vectors  $\mathbf{u}$  defined by  $\mathbf{u} = \cos\theta\hat{z} + \sin\theta\cos\phi\hat{x} + \sin\theta\sin\phi\hat{y}$ ,  $\mathbf{u}_\phi = \hat{z} \times \mathbf{u}$ , and  $\mathbf{u}_\theta = \mathbf{u} \times \mathbf{u}_\phi$ . The incident field on the mirror is cast as a sum of monochromatic plane waves [see Fig. 1(a)], propagating in the  $\mathbf{u}$  direction with complex amplitude vector  $\mathbf{e}(\mathbf{u})$ :

$$\mathbf{E}_{\text{inc}}(\mathbf{r}) = \int_0^{2\pi} d\phi \int_{-\theta_{\text{max}}}^{\theta_{\text{max}}} d\theta \sin\theta \mathbf{e}_i(\mathbf{u}) \exp(ik_0\mathbf{u} \cdot \mathbf{r}), \quad (1)$$

where  $k_0 = 2\pi/\lambda$  is the wavenumber in the sample space and  $\theta_{\text{max}}$  is the maximum angle that can be reached in the sample space with the chosen numerical aperture of the objective. Because of the transverse nature of the plane waves,  $\mathbf{e}_i(\mathbf{u})$  can be decomposed on the  $(\mathbf{u}_\theta, \mathbf{u}_\phi)$  basis. Assuming the mirror to be perfectly conducting, the reflected beam reads

$$\mathbf{E}_{\text{refl}}(\mathbf{r}) = \int_0^{2\pi} d\phi \int_{-\theta_{\text{max}}}^{\theta_{\text{max}}} d\theta \sin\theta \mathbf{e}_r(\mathbf{u}) e^{ik_0[\mathbf{u} - 2(\mathbf{u} \cdot \hat{z})\hat{z}] \cdot \mathbf{r}}, \quad (2)$$

where  $\mathbf{e}_r(\mathbf{u}) = -\mathbf{e}_i(\mathbf{u}) + 2[\mathbf{e}_i(\mathbf{u}) \cdot \hat{z}]\hat{z}$  and  $\cdot$  stands for the scalar product.

The shaping of the incident beam is performed following the time-reversal focusing theory depicted in [26] and illustrated in Fig. 1. To focus light at the point  $\mathbf{r}_0 = z_0\hat{z}$ ,  $\mathbf{e}_i(\mathbf{u})$  should ideally be equal to the complex conjugate of  $\mathbf{e}_p(-\mathbf{u})$ , the complex amplitude vector of the plane wave emitted in the  $-\mathbf{u}$  direction by a dipole source  $\mathbf{p}$  placed at  $\mathbf{r}_0$ . The radiation of the dipole in front of the mirror is equivalent to that of two dipoles in free space, symmetrically positioned with respect to the mirror plane at  $z_0$  and  $-z_0$ , with the same  $z$  component and opposite  $(x, y)$  components. As a result, one finds for  $\mathbf{p}$  parallel to the mirror

$$\mathbf{e}_i^{\text{ideal}}(\mathbf{u}) \propto \sin(z_0k_0 \cos\theta)[\mathbf{p} - (\mathbf{p} \cdot \mathbf{u})\mathbf{u}], \quad (3)$$

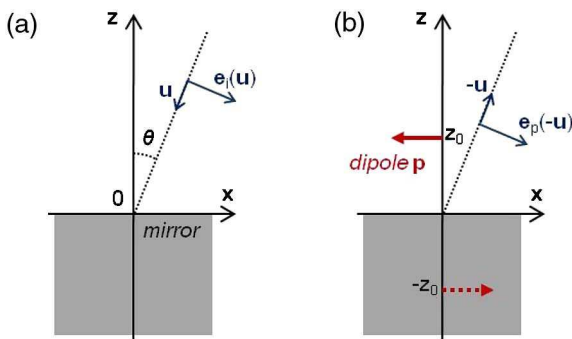


Fig. 1. (Color online) Illustration of the ISO focusing concept, based on the time-reversal theory. (a) The incident field is made of a sum of plane waves propagating along  $\mathbf{u}$  with complex vector amplitude  $\mathbf{e}_i(\mathbf{u})$ . (b) The field radiated by a dipole placed at  $z_0\hat{z}$  before the mirror can be decomposed as a sum of plane waves propagating along  $-\mathbf{u}$  with complex vector amplitude  $\mathbf{e}_p(-\mathbf{u})$ . To focus at point  $z_0\hat{z}$ , the time-reversal focusing theory states that  $\mathbf{e}_i(\mathbf{u})$  should ideally be equal to the conjugate of  $\mathbf{e}_p(-\mathbf{u})$ .

and the same expression with  $\sin(z_0k_0 \cos\theta)$  replaced by  $\cos(z_0k_0 \cos\theta)$  for a dipole normal to the mirror. Note that the incident beam  $\mathbf{E}_{\text{inc}}$  defined by Eq. (1) with  $\mathbf{e}_i$  given by Eq. (3) focuses at two points along the optical axis, at  $z_0$  and  $-z_0$ . The shape of the two spots is elongated along the optical axis in the same way as that of the standard spot obtained by focusing a plane wave through one objective lens. The quasi-isotropic spot is obtained through the interference between the incident and the mirror-reflected beams.

More precisely, if  $\theta_{\text{max}} = \pi/2$ , the time-reversal theory states that the total field,  $\mathbf{E}_{\text{tot}}(\mathbf{r}, \mathbf{r}_0) = \mathbf{E}_{\text{inc}}(\mathbf{r}, \mathbf{r}_0) + \mathbf{E}_{\text{refl}}(\mathbf{r}, \mathbf{r}_0)$  with  $\mathbf{e}_i$  satisfying Eq. (3), is proportional to the imaginary part of the electric field radiated by the dipole placed at  $\mathbf{r}_0$  before the mirror [26]. Now, because of the rapid decay of the reflected field (namely the field emitted by the image dipole), the field radiated by the dipole before the mirror is quite similar to the field radiated by the same dipole in free space. Its intensity distribution has a quasi-spherical shape with radius at half-maximum about  $\lambda/2$ . Hence, the time-reversal beam shaping appears as a very efficient way of obtaining an isotropic light spot that can be moved with respect to the mirror, without distortion, just by changing  $z_0$  in Eq. (3).

### B. Simulation of the PSF of the ISO Microscope

Considering a realistic objective lens,  $\theta_{\text{max}}$  is inevitably smaller than  $\pi/2$ . Moreover, it is generally difficult to shape simultaneously the phase, amplitude, and polarization of the incident waves to obtain a field satisfying Eq. (3). Hence, to investigate the achievable performances of the ISO focusing and imaging concept, we have performed simulations of the illumination and global PSF of the ISO microscope accounting for these constraints.

In our experimental configuration, a spatial light modulator (SLM) that only modifies the phase of the field is placed at (or conjugated to) the rear focal plane of a microscope objective lens. The first difficulty is to relate the field leaving the SLM plane to the plane waves that illuminate the mirror.

To indicate points and vectors in the  $(x, y)$  SLM plane, we introduce the cylindrical set of coordinates  $(\rho, \psi)$  associated to the local basis  $(\mathbf{u}_\rho = \cos\psi\hat{x} + \sin\psi\hat{y}, \mathbf{u}_\psi = -\sin\psi\hat{x} + \cos\psi\hat{y})$ . Under Abbe's sine condition, a point  $(\rho, \psi)$  of the rear focal plane (where the SLM is placed) corresponds to a plane wave propagating in the sample space along the  $\mathbf{u}$  direction defined by the polar and azimuthal angles  $(\theta, \phi)$  that satisfy  $\phi$  equal to  $\psi$  and

$$\sin\theta = (\sin\theta_{\text{max}})\rho/R, \quad (4)$$

where  $R$  is the radius of the aperture at the rear side of the objective lens. More precisely, provided that we can neglect the various reflections on the optical components, the electric field  $\mathbf{E}(\rho, \psi)$  collinear to  $[\mathbf{u}_\phi, \mathbf{u}_\rho]$  leaving the SLM plane at point  $(\rho, \psi)$  is transformed into a plane wave propagating along  $\mathbf{u}$  that is polarized along  $\mathbf{u}_\psi[-\mathbf{u}_\theta]$  with a damped modulus  $E(\rho, \psi)\sqrt{\cos\theta}$ , where  $\sqrt{\cos\theta}$  is the so-called aplanatic factor. Hence, the complex amplitude vectors of the incident plane waves in the sample space that are generated by any field  $\mathbf{E}(\rho, \psi)$  leaving the SLM read

$$\mathbf{e}_i(\mathbf{u}) = \sqrt{\cos\theta}\{[\mathbf{E}(\rho, \psi) \cdot \mathbf{u}_\phi]\mathbf{u}_\psi - [\mathbf{E}(\rho, \psi) \cdot \mathbf{u}_\rho]\mathbf{u}_\theta\}. \quad (5)$$

Equation (5) gives the field in an aberration-free system satisfying the sine condition. Other apodization factors could be used (to account, for example, for the Fresnel transmission coefficients of the lens), but they were shown to have a limited impact on the size of the PSF [27]. The field leaving the SLM,  $\mathbf{E}(\rho, \psi)$ , can be written as  $\mathbf{E}(\rho, \psi) = \mathbf{E}_0(\rho, \psi) \exp[if(\rho, \psi)]$ , where  $\mathbf{E}_0(\rho, \psi)$  is the incident field on the SLM and  $f(\rho, \psi)$  is the phase modulation applied by the SLM. In our setup, the SLM is illuminated by a collimated beam that is linearly polarized along the  $x$  axis, which corresponds to the working axis of the SLM. Hence,  $\mathbf{E}_0$  is a constant. The pattern displayed on the SLM is given by the phase of Eq. (3):

$$f(\rho, \psi) = \frac{\pi}{2} \text{sign}[\sin(z_0 k_0 \cos \theta)], \quad (6)$$

where  $\theta$  is related to  $\rho$  through Eq. (4). Introducing Eq. (6) into Eq. (5) and comparing the latter to Eq. (3) with  $\mathbf{p} = \hat{\mathbf{x}}$ , one observes that the phase of  $e_i$  coincides with that obtained for  $e_i^{\text{ideal}}$ . On the other hand, the modulus and polarization differ, especially for large  $\theta$  and for propagation directions outside the  $(x, z)$  or  $(y, z)$  planes, but the consequences on the focusing are negligible [28].

Once the complex vector amplitudes of the plane waves forming the incident beam are well defined, we calculate the reflected beam with Eq. (2). The total field  $\mathbf{E}_{\text{tot}}(\mathbf{r}, \mathbf{r}_0) = \mathbf{E}_{\text{inc}}(\mathbf{r}, \mathbf{r}_0) + \mathbf{E}_{\text{refl}}(\mathbf{r}, \mathbf{r}_0)$  depends on the chosen focal point  $\mathbf{r}_0$  via the phase pattern displayed on the SLM, Eq. (6). Yet we have checked numerically that, except when  $\mathbf{r}_0$  is close to the mirror (typically for distances smaller than half the wavelength), the spot shape does not vary when  $\mathbf{r}_0$  is changed. In other words, the illumination PSF,  $\text{PSF}_{\text{ill}}(\mathbf{r} - \mathbf{r}_0) \propto |\mathbf{E}_{\text{tot}}(\mathbf{r}, \mathbf{r}_0)|^2$  can be assumed to be homogeneous within the sample space.

Now, to perform a complete modeling of the experiment, one needs to simulate the image of a pointlike fluorescent source placed at  $\mathbf{r}$  in the sample space. In our setup, we use a confocal detection scheme. The fluorescence light is modified by the SLM and polarized along the  $x$  axis in the same way as the incident light before being sent, through a pinhole, onto a detector. We assume that the intensity recorded by the detector is proportional to  $\int_S d\mathbf{v} |\mathbf{E}(\mathbf{v}) \cdot \hat{\mathbf{x}}|^2$ , where  $S$  is the pinhole transmission area and  $\mathbf{E}(\mathbf{v})$  is the field radiated at point  $\mathbf{v}$  by the fluorescent dipole  $\mathbf{p}_{\text{fluo}}$  placed at  $\mathbf{r}$  in the sample space for a given focal point  $\mathbf{r}_0$  set on the SLM.

The calculation of  $\mathbf{E}(\mathbf{v}) \cdot \hat{\mathbf{x}}$  is easily done by invoking the reciprocity theorem [29]. We consider a virtual monochromatic dipole  $\mathbf{p}_{\text{virtual}}$ , oriented along the  $x$  axis, placed at the center of the pinhole and radiating at the same wavelength as the fluorescent dipole,  $\lambda'$ , which is slightly different from the wavelength of the illumination  $\lambda$ . It generates a plane wave normal to the SLM plane and creates, in the sample space, the field  $\mathbf{E}'_{\text{tot}}(\mathbf{r}, \mathbf{r}_0)$ . If  $\mathbf{p}_{\text{virtual}}$  is shifted by  $\mathbf{v}$  in the pinhole plane, it creates the field  $\mathbf{E}'_{\text{tot}}(\mathbf{r}, \mathbf{r}_0 + \mathbf{v})$  in the sample space (for simplicity, we overlook the magnification factors between the pinhole and the sample space). The reciprocity theorem states that  $\mathbf{E}(\mathbf{v}) \cdot \mathbf{p}_{\text{virtual}} = \mathbf{p}_{\text{fluo}} \cdot \mathbf{E}'_{\text{tot}}(\mathbf{r}, \mathbf{r}_0 + \mathbf{v})$ . Now, the fluorescent dipole amplitude is proportional to the field at point  $\mathbf{r}$  created by the incident laser field  $\mathbf{E}_{\text{tot}}(\mathbf{r}, \mathbf{r}_0)$ . Finally, the intensity recorded by the detector can be written as

$$I(\mathbf{r}, \mathbf{r}_0) \propto \text{PSF}_{\text{ill}}^{\lambda}(\mathbf{r} - \mathbf{r}_0) \text{PSF}_{\text{det}}^{\lambda'}(\mathbf{r} - \mathbf{r}_0), \quad (7)$$

where  $\text{PSF}_{\text{det}}^{\lambda'}(\mathbf{r} - \mathbf{r}_0) = \int_S d\mathbf{v} \text{PSF}_{\text{ill}}^{\lambda'}(\mathbf{r} - \mathbf{r}_0 - \mathbf{v})$ . We note that  $I(\mathbf{r}, \mathbf{r}_0)$  depends solely on  $\mathbf{r} - \mathbf{r}_0$ . We then introduce the global PSF of the microscope,  $\text{PSF}(\mathbf{r} - \mathbf{r}_0) \propto I(\mathbf{r}, \mathbf{r}_0)$ , which, in the ideal case of a point detector and a perfectly coherent fluorescent source emitting at the same wavelength as the excitation light, is equal to  $\text{PSF}_{\text{ill}}^2$ . This ideal configuration is equivalent to a 4Pi microscope of type C with a point detector [30]. Unfortunately, the fluorophore emits at a longer wavelength than the excitation wavelength and, more important, the coherence length of the emitted light is about  $3 \mu\text{m}$ , which is generally smaller than the distance between the fluorescent source and the mirror. As a result, the fluorescent light directly emitted toward the objective lens does not interfere with the emitted light that is reflected by the mirror before being collected. In this case,  $|\mathbf{E}'_{\text{tot}}(\mathbf{r}, \mathbf{r}_0)|^2 = |\mathbf{E}'_{\text{inc}}(\mathbf{r}, \mathbf{r}_0)|^2 + |\mathbf{E}'_{\text{refl}}(\mathbf{r}, \mathbf{r}_0)|^2$  and the detection PSF is very similar to that of a conventional confocal microscope. This configuration corresponds to a 4Pi A-type microscope [30]. Note that, by placing a filter (with typically a 10 nm bandpass) in front of the pinhole, one could increase the coherence length of the fluorescence light so that the direct and reflected beams interfere. In this case, the detection PSF would be similar to the illumination PSF and the configuration would correspond to a 4pi-C microscope.

Figure 2 shows the global PSF of the ISO microscope, calculated for a quasi-ideal objective with  $\sin \theta_{\text{max}} = 0.99$  and a more realistic one with  $\sin \theta_{\text{max}} = 0.80$ . In these calculations, we use the parameters of the experimental setup: wavelength  $\lambda = 491 \text{ nm}$  and pinhole diameter in the focal plane  $1.22\lambda$ . Light is focused in vacuum and the objective lens is assumed to be ideally unaberrated. The validity of our numerical technique was checked by comparing its results for a standard confocal microscope to the semianalytical expressions given in [31]. The SLM is modeled as a  $1000 \times 1000$  pixel array, with a constant phase value on each pixel. To account for possible errors stemming from the SLM pixelization, the propagation directions of the plane waves forming the incident beam are not discretized in the Cartesian SLM basis but in the spherical basis  $(\theta, \phi)$ , 500 in  $\theta$  and 180 in  $\phi$ . The SLM pattern is tuned to focus light at  $z_0 = 20\lambda$  from the mirror and the incident polarization is collinear to the  $x$  axis. The fact that the emission

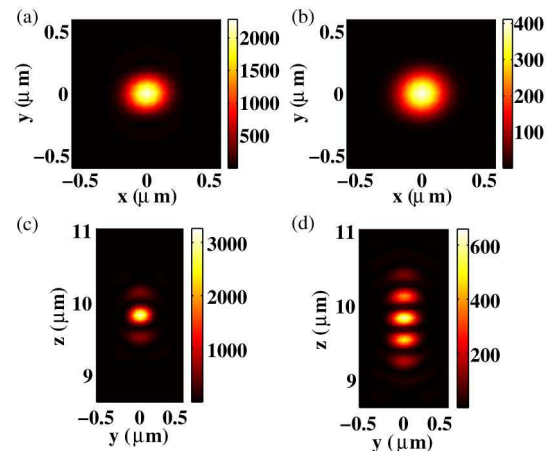


Fig. 2. (Color online) Global PSF of an ISO microscope, simulated for two different objectives in air: (a) and (c) ideal objective with  $\text{NA} = \sin \theta_{\text{max}} = 0.99$ ; (b) and (d) realistic objective,  $\text{NA} = \sin \theta_{\text{max}} = 0.80$ . These images correspond to slices taken in the (a), (b) transverse and (c), (d) axial planes.

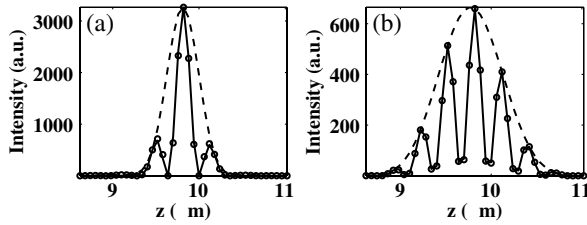


Fig. 3. Axial profiles taken from the PSF of an ISO microscope (solid curve) and a conventional confocal microscope (dashed curve), simulated for different NA in vacuum. (a) NA = 0.99. (b) NA = 0.80. For comparison purposes, the PSF of the conventional confocal microscope has been plotted after modulation by  $\cos^2[\beta k_0(z - z_0)]$  (circles). The observed dissymmetry stems from the phase mask discretization induced by the SLM.

wavelength differs from the excitation one is not taken into account for these simulations.

The global PSF obtained for NA = 0.99 is quasi-isotropic with diameter of about  $\lambda/3$ . For NA = 0.8, the central peak of the PSF is also quasi-isotropic, but it is plagued by sidelobes of higher relative intensity (60% to 80% of the main lobe) than that observed for NA = 0.99 (about 20%).

Remarkably, we observe that, along the optical axis, the global PSF<sub>tot</sub> of the ISO microscope is perfectly fitted by the global PSF<sub>tot</sub> of the conventional confocal microscope (with same numerical aperture) times  $\cos^2[\beta k_0(z - z_0)]$ . The parameter  $\beta$  depends on the numerical aperture of the objective (0.70 for NA = 0.99 and 1.02 for NA = 0.80); see Fig. 3. This behavior is easily understood if one approximates the ISO spot by the interference of two counterpropagative Gaussian beams with superimposed waists. The parameter  $\beta$  indicates that, along the optical axis, the phase of the field forming the beams does not vary along  $z$  as  $k_0 z$ . Indeed, there exists a phase delay, known as the Gouy phase (which depends on the beam waist and thus on the numerical aperture of the objective), that modifies the period of the interference pattern. This property gives an interesting self-consistent way to verify that the ISO microscope is correctly tuned as it relates the ISO

PSF to the standard confocal one obtained with the same objective. In the following, we will use this approach rather than a direct comparison between theory and experiment to assess the accuracy of our mounting. Indeed, we noticed that comparing theoretical results to experimental ones was particularly difficult as the claimed numerical aperture and apodization functions of the objective were not those observed experimentally [32].

### C. Discussion of the Phase Pattern

In the absence of the mirror, the incident beam described in Eqs. (1) and (3) focuses at two points, located at  $z_0$  and  $-z_0$  along the optical axis. Therefore, an alternative approach to time-reversal focusing could consist in splitting the SLM in two and displaying two Fresnel lenses focusing at different points. The phase pattern of each Fresnel lens is then  $f(\rho, \psi) = k_0 z_0 \cos \theta$  for the first one and  $f(\rho, \psi) = -k_0 z_0 \cos \theta - \pi$  for the second one. The  $-\pi$  added to this second formula is necessary to obtain the correct phase match between these two focuses. The advantage of the Fresnel lens mask is that it can generate spots that are as close to each other as possible, whereas the time-reversal mask becomes very approximate when  $z_0$  decreases below a given value. In fact, as  $z_0$  tends to 0, the number of sign changes in the function  $\sin(z_0 k_0 n \cos \theta)$  tends to 0, too, and therefore the phase modulation becomes increasingly less efficient to substitute for an ideal amplitude modulation in the time-reversal approach. The disadvantage of the Fresnel lens mask is that it requires splitting the SLM in two areas so that only part of the  $\mathbf{u}$  directions focus at  $z_0$  ( $-z_0$ ). In Fig. 4, we give an example of the phase masks that are displayed on the SLM following the time-reversal technique or the Fresnel lens approach with different templates for splitting the SLM. All three masks shown in Fig. 4 were designed for focusing light at  $z_0 = 1 \mu\text{m}$  (with  $\lambda = 491 \text{ nm}$ ). The simulations of the global PSF obtained with these different masks were very similar (not shown).

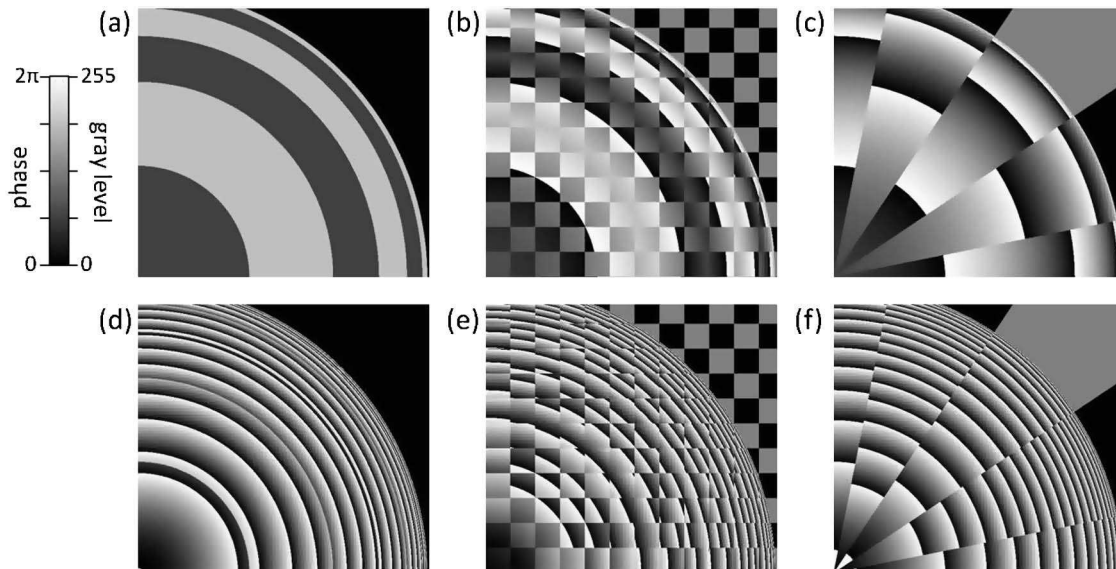


Fig. 4. Examples of phase masks for ISO focusing. For symmetry reasons, only the top right quarter of the masks are shown (bottom left corner is the center of symmetry). Mask designs are based on (a) and (d) the principle of time-reversal focusing and (b), (c), (e), and (f) combinations of Fresnel phase plates following (b), (e) a checkerboard of  $50 \times 50$  pixel squares and (c), (f) a pie chart of 16 slices. These masks were generated for two different configurations in which the mirror is placed (a)–(c) in the genuine focal plane of the objective lens and (d)–(f) at  $d = 6 \mu\text{m}$  above it. In the latter case, the term  $k_0 d \cos \theta$  has been added to all the phase patterns given in the text.

We now turn to the experimental measurement of the global PSF of the ISO microscope. In our experimental setup, we have used both the time-reversal and Fresnel lens techniques for engineering the incident beam.

### 3. EXPERIMENTAL RESULTS

#### A. Description of the Setup

The experimental configuration of the microscope exhibits the same features as those presented in Section 2. Basically, the ISO microscope consists of a conventional home-built confocal microscope that has been modified to allow the wavefront shaping of the incident and detected light; see Fig. 5. More precisely, a phase-only SLM (Pluto-VIS, Holoeye) functioning in reflection was introduced between a dichroic mirror (z488/633, Chroma) and a water-immersion objective lens (Plan Apo VC 60 $\times$ , NA = 1.2, Nikon). The SLM plane was optically conjugated to the rear focal plane of the lens using a telescope. Hence, each pixel of the SLM corresponded to one direction in the observation region as assumed in Section 2. Excitation was supplied by a continuous wave 491 nm laser. The fluorescence light collected in epi-illumination was “descanned” by the SLM in order to keep the optical conjugation between the pinhole and the probed region. It was spectrally filtered (FF01-525/39-25, Semrock, center wavelength 525 nm, bandwidth 39 nm at 90% transmittance or 45 nm at 50% transmittance, corresponding to a coherence length of about 3  $\mu$ m in vacuum) and spatially filtered with a 30  $\mu$ m pinhole (i.e., 1 Airy diameter) placed in front of a photon counter (PD1C0C, Micro Photon Devices). Both excitation and fluorescence lights were horizontally polarized (along the  $x$  axis) so as to be parallel to the working axis of the SLM. Typical excitation power and acquisition dwell time were 10  $\mu$ W and 1 ms/pixel, respectively.

The sample consisted in a suspension of isolated 100 nm spheres (FluoSpheres yellow/green, Invitrogen) in a 1 wt. %

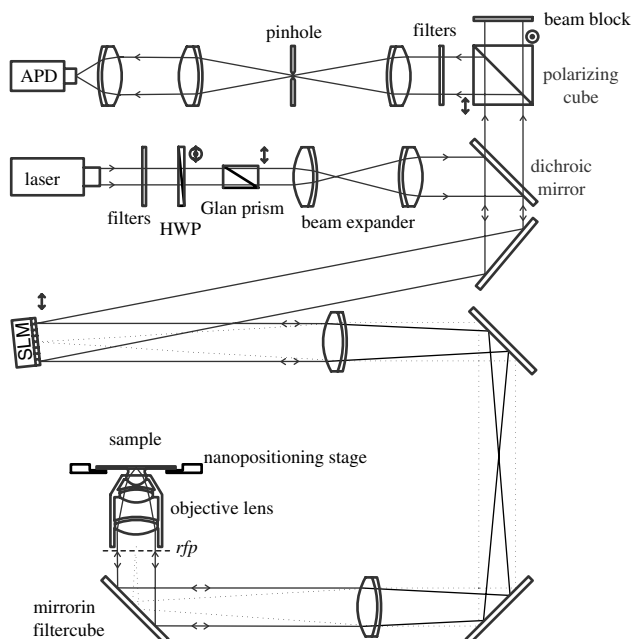


Fig. 5. Schematic of the microscope setup. APD, avalanche photodiode; HWP, half-wave plate; SLM, phase-only spatial light modulator; rfp, rear focal plane. Lenses are achromatic doublets. See details in text.

agarose gel film (typical thickness of 5 to 10  $\mu$ m) and was sandwiched between an Ag coated mirror and a conventional 150  $\mu$ m coverslip. The mirror was placed a few micrometers away from the focal plane of the microscope objective lens on a nanopositioning stage (NanoLP100, Mad City Labs). In our configuration, axial scanning was performed by changing the SLM pattern, while transverse scanning was done by translating the mirror in the ( $x, y$ ) plane with the stage.

#### B. Global PSF of the ISO Microscope

To estimate the global PSF of the ISO microscope, we measured 3D images of isolated beads in the sample and assumed that the latter were small enough to be considered pointlike sources. Although a more precise assessment of the PSF would require 3D deconvolution of the image by the bead volume, we found by numerical simulations that the actual bead size (100 nm) only slightly affects the fringe contrast. Different patterns were displayed on the SLM to engineer the wavefront. The best results were obtained for the time-reversal mask [see Fig. 6(a)] and the Fresnel mask with a 16 slice pie-chart template [see Fig. 6(b)]. We observed that the performance of the checkerboard templates decreased with the square size (from 50  $\times$  50 pixels to 1  $\times$  1 pixel). The influence of the templates on the experimental image, which is not retrieved with the simulations, points out the practical limits of the SLM and, in particular, its failure to generate important phase changes at high spatial frequency; see Appendix A for more details.

To check the performance of the ISO setup, we compared the image of a bead obtained in the ISO configuration to that of a bead measured in the conventional confocal geometry

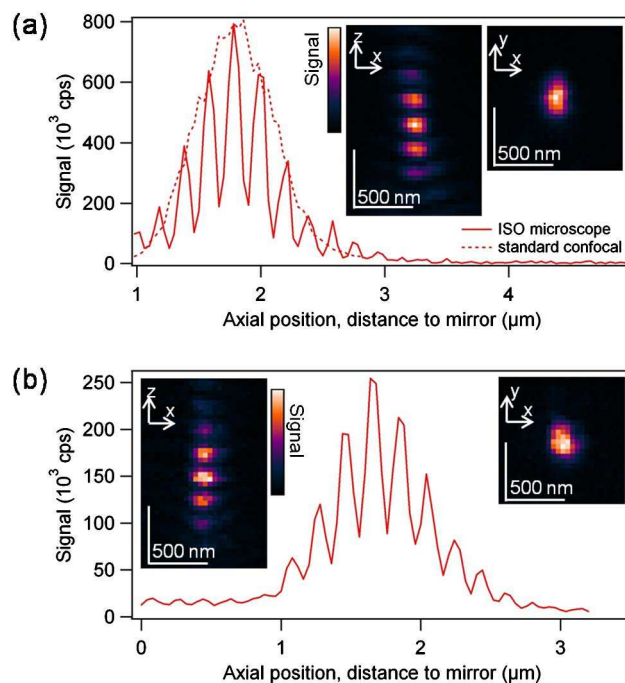


Fig. 6. (Color online) Profile intensity along the  $z$  axis of the images of isolated 100 nm fluorescent beads, measured by ISO microscopy. Vertical and horizontal slices of these images are shown in insets. Phase mask designs were based on (a) time-reversal and (b) combinations of Fresnel phase plates with respect to a pie chart of 16 slices; see Fig. 4. Note that the image of the bead was recorded by transverse scanning with the nanopositioning stage and axial scanning of the sample with the SLM.

(i.e., without the mirror and the SLM); see Fig. 6(a). Similar to the simulated PSF shown in Section 2, we observed that the experimental ISO PSF is close to the experimental PSF of the conventional confocal microscope, modulated by  $\cos^2[\beta k_0(z - z_0)]$ . We thus obtain a quasi-isotropic central peak, flanked by high sidelobes that reflect the less than perfect focusing achievement of the conventional confocal microscope.

We then checked the homogeneity of the global PSF, by studying the images of beads located at various distances from the mirror (Fig. 7). We observed that, as expected, the profiles exhibit the same features whatever the distance of the bead to the mirror and the positions of the fringes change with the location of the beads.

These experimental results suggest that we have achieved the finest ISO PSF possible with such a confocal microscope. It is worth noting that, even for experiments requiring 15 to 20 min long measurements, we observed no drift of the setup; namely, the ISO PSF was preserved all along. We now describe the preliminary studies that were necessary to tune properly the ISO setup and obtain these results.

### C. Tuning an ISO Microscope, Cautions, and Preliminary Studies

Basically, the ISO setup requires checking three important steps: the confocal detection, the engineering of the wavefront, and the mirror positioning.

#### 1. Confocal Detection

We have seen in Section 2 that ISO microscopy requires that both incident excitation light and collected fluorescence light be treated by the SLM; otherwise, it would not be compatible with a confocal detection scheme. Now, fluorescence light has a slightly longer wavelength than that of the excitation light, for which the phase masks were designed. Because of this chromatism issue, we expect the optimal position of the pinhole to slightly change when going through the phase mask

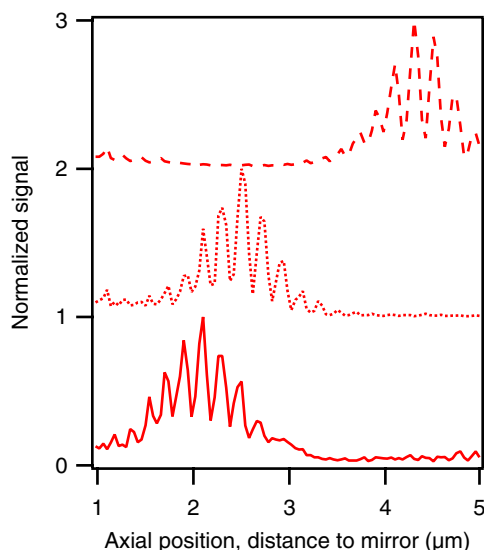


Fig. 7. (Color online) Intensity profiles taken along the axial direction of 3D images of 100 nm fluorescent beads, measured by ISO microscopy using time-reversal phase masks. Bead-to-mirror distances are estimated, on the basis of the position of the brightest fringe in the interference patterns, to 2.1  $\mu\text{m}$  (solid curve), 2.5  $\mu\text{m}$  (dotted curve), and 4.3  $\mu\text{m}$  (dashed curve).

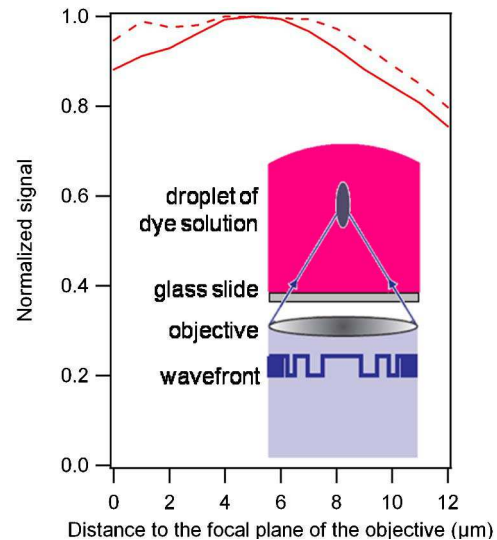


Fig. 8. (Color online) Relative variation of the fluorescent signal as a function of the phase masks displayed on the SLM, measured by focusing light in a droplet of fluorescent dye solution (Rhodamine 6G). Fresnel-lens phase masks were used to focus light in a single spot 0 to 12  $\mu\text{m}$  before the genuine focal plane of the objective lens. Spatial filtering at detection was performed with pinholes of diameter 30  $\mu\text{m}$  (solid curve) and 50  $\mu\text{m}$  (dashed curve). These curves reveal the dependence of the detection sensitivity on the SLM display.

series. Therefore, we evaluated the detection efficiency of the microscope for each of the phase masks, by focusing light in a droplet of fluorescent dye solution (Rhodamine 6G,  $10^{-6} \text{ mol l}^{-1}$ ), as schematized in Fig. 8. The position of the pinhole was optimized while focusing light 6  $\mu\text{m}$  before the focal plane. We observed that the detection efficiency decays slowly as the focus is moved away by displaying different masks on the SLM. Loss of efficiency is observed down to about 20% at the extremes. Unsurprisingly, we found that the decay depends on the size of the pinhole; larger pinholes yield smaller losses. A pinhole of diameter 30  $\mu\text{m}$  (i.e., 1 Airy diameter) appeared to be a fair trade-off between the optical sectioning and a relatively constant efficiency of detection over a sufficiently wide scanning range along the optical axis.

#### 2. Engineering the Wavefront of the Incident Beam

In a simplified view, ISO focusing consists in forming two spots along the optical axis, one at the focal position and the other at its virtual image behind the mirror. Hence, at least one of them forms out of the genuine focal plane of the objective lens. Now, for achieving an interference pattern of optimal contrast, the two spots should have a similar field distribution and be accurately positioned. Hence, it is necessary to check that focusing out of the focal plane does not deteriorate the spots. We tested the ability of our water-immersion microscope objective to focus light up to 12  $\mu\text{m}$  before its focal plane by displaying a Fresnel lens with varying focal length on the SLM. This was done by recording images of beads scattered in an agarose gel film deposited on a standard glass slide. Axial slices of these images are shown in Figs. 9(a) and 9(b). Spot radii at  $1/e^2$  (see Fig. 9) were then evaluated by fitting axial and transverse profiles taken from the image with a Gaussian function. Axial and transverse widths were found almost constant (to within 0.03  $\mu\text{m}$ ), which indicates that focusing out of the focal plane by wavefront shaping with simple

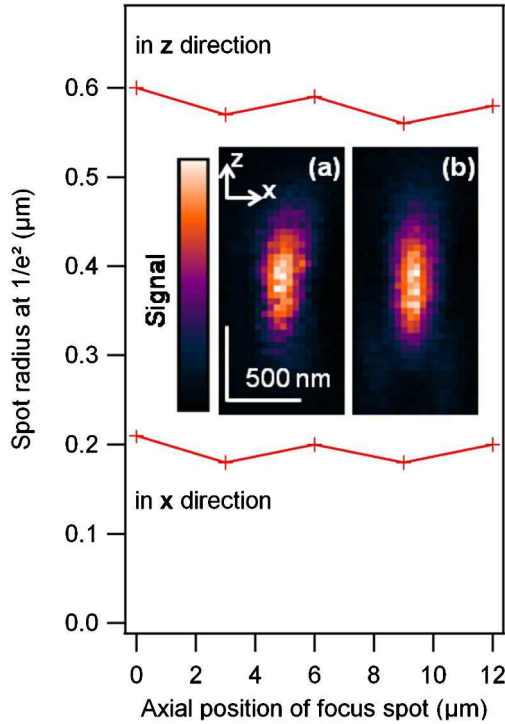


Fig. 9. (Color online) Spot radii at  $1/e^2$ , evaluated by fitting (with a Gaussian curve) axial and transverse profiles taken from fluorescence images of a 100 nm bead, measured while controlling the actual plane where light focuses using the SLM. Inset: axial slices of two of these images, measured while focusing (a) in the genuine focal plane of the lens and (b) in a plane located  $12\ \mu\text{m}$  before it.

Fresnel phase masks introduces only negligible aberrations, within  $12\ \mu\text{m}$  (at least) before the focal plane of the objective.

We decided to place the mirror at  $d = 6\ \mu\text{m}$  before the genuine focal plane of the objective in order to minimize the influence of the incident light that is unaffected by the SLM, which then focuses behind the mirror. The phase masks were then designed to generate two spots at equidistant locations with respect to a plane that lays at  $d = 6\ \mu\text{m}$  before the genuine focal plane (see Fig. 4) and their axial range was limited to  $6\ \mu\text{m}$  above and below this plane to remain within the checked aberration-free domain. Hence, in all the experiments, the samples were axially scanned over a layer of  $6\ \mu\text{m}$  before the mirror only.

The phase mask building also required some cautions. In order to apply the time-reversal formulas or to arrange a combination of Fresnel lenses in a mask, one needs to associate the pixels of the SLM [defined by their coordinates  $(\rho, \psi)$ ] to the propagation directions  $\mathbf{u}$  after the objective lens. The main difficulty is to determine the radius  $R$  of the pupil image on the SLM as introduced in Eq. (4). First, an approximate value of  $R$  can be calculated from the specifications of the objective lens (numerical aperture and radius of the pupil) and the magnification ratio brought by the telescope between the SLM and the objective lens. Then, this value of  $R$  can be refined through a simple calibration method that consists in measuring the 3D image of a fluorescent bead (in the absence of the mirror) while displaying on the SLM a phase mask for ISO focusing. In that case, axial scanning is performed with the stage. The phase mask is designed to generate a spot at a given distance  $z_0$  to the mirror and yields two spots separated by  $2z_0$  along the optical axis in the absence of the mirror. The image

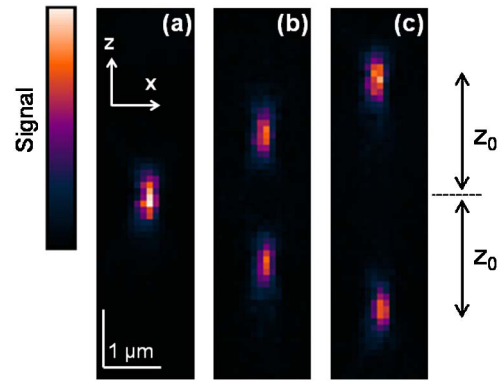


Fig. 10. (Color online) Fluorescence images (axial slices) of a 100 nm bead, measured with time-reversal phase masks that yield pairs of spots separated by (a) 0, (b) 2, and (c)  $4\ \mu\text{m}$  along the optical axis in the absence of the mirror.

reveals the positions of the two spots and the radius  $R$  is optimized until the distance between the two spots actually corresponds to two times the targeted  $z_0$ . Figures 10(b) and 10(c) show vertical slices in an axial plane of the bead image, measured with phase masks designed with the time-reversal approach for  $z_0 = 1$  and  $2\ \mu\text{m}$ . After calibration, the image reveals pairs of spots that are separated by  $2z_0 = 2$  and  $4\ \mu\text{m}$  along the optical axis, as expected.

### 3. Placing the Mirror

Once the two twin spots are created, we axially scan the mirror through focus and measure the detected signal strength. This technique permits one to localize the two spots with

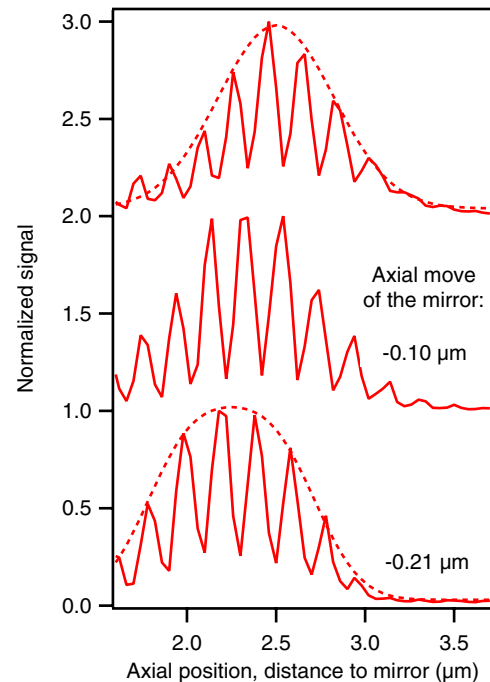


Fig. 11. (Color online) Three intensity profiles, taken in the axial direction from fluorescence images of a single 100 nm bead, for different positions of the mirror. In the middle and bottom profiles, the mirror position differs by 0.10 and  $0.21\ \mu\text{m}$  from that of the top profile, respectively. Top and bottom profiles are fitted with envelope curves (dashed curve) corresponding to (top) a Gaussian function of radius  $0.65\ \mu\text{m}$  at  $1/e^2$  and (bottom) a sum of two identical Gaussian functions of same radius  $0.65\ \mu\text{m}$  but of different centers.

accuracy. The mirror is then placed at equidistance of the spots with the stage. A slight tilt of the mirror, if any, can be very accurately corrected by translating the center of the phase mask on the SLM. Namely, its translation by one pixel in either the  $x$  or  $y$  directions (i.e., by  $8\ \mu\text{m}$ ) equates in first approximation to a tilt correction by about  $0.1^\circ$ . The accurate positioning of the mirror is crucial as it governs the overlapping of the spots.

To investigate the sensitivity of the ISO PSF to possible mispositioning or drifts of the mirror, we measured the image of a bead for different positions of the mirror. As shown in Fig. 11, the alteration of the PSF is obvious for shifts of  $0.10\ \mu\text{m}$  or larger. Thus, mechanical drifts above  $100\ \text{nm}$  are expected to significantly deteriorate the PSF. Now, we found that, although we did not use any additional stabilizing system, measurements of 15 to 20 min could be conducted without seeing any deterioration of the PSF. Hence, we believe that the stability of the mirror position within  $100\ \text{nm}$  over the experiment time is not an issue.

#### 4. CONCLUSION

We presented a novel epifluorescence confocal microscopy technique, called ISO microscopy, in which the sample is laid on a mirror and scanned by a quasi-isotropic spot that is formed through the interference of the direct and mirror-reflected field of a specially shaped illumination beam. We have shown theoretically and experimentally that the PSF of this system is similar to that of a 4pi-A microscope. It displays a quasi-isotropic spot of diameter about  $\lambda/2$  surrounded by high sidelobes. To diminish the amplitude of the latter and make the system convenient for imaging, a microscope objective with an acceptance solid angle of about  $74\ \text{deg}$  should be used [33]. Other areas of improvements are the development of a 4pi-C equivalent ISO scheme or the use of two-photon excitation.

#### APPENDIX A: CORRECTION AND CALIBRATION OF THE SPATIAL LIGHT MODULATOR

The technology of our SLM (liquid crystals on silicon chip) has the disadvantage that it makes displays of relatively poor surface flatness, which may degrade the incident wavefront and alter the ability of the microscope to focus light. Therefore, we did a complete diagnosis of these aberrations by analyzing the reflection of coherent light by the SLM using a wavefront sensor (SID-4 HR, Phasics) mounted on the microscope at the position of the rear focal plane of the objective lens. We found that the curvature of the SLM mainly introduced defocus and astigmatism, as well as spherical aberrations to a lower extent. We compensated for defocus and astigmatism by finely adjusting the axial and lateral positions of the lenses in the setup. This was achieved while keeping all optical planes conjugated and it allowed us to reach wavefront RMS flatness lower than 0.1 times the wavelength of light. The remaining spherical aberrations were minimized by finely adjusting the objective correction collar while monitoring the aspect of the focal spot on a reflective interface of the sample. As an alternative to compensate for the SLM curvature, we also exploited the wavefront analysis to calculate a "correction map" that can be added to any phase mask on the SLM. However, the first option (i.e., handling the "physical" lenses of the

setup) has the advantage over the second one that the confocal microscope can still be operated in conventional mode (i.e., without wavefront shaping) simply by switching off the SLM.

We configured the SLM to have a linear relationship between the signal sent to its driving unit and the phase shift actually experienced by the reflected light. For this purpose, we measured the phase characteristic of the SLM in an interferometric setup. Then we inverted it to obtain a new data lookup table for the driving unit, in order to have a linear phase response within a well-defined  $0-2\pi$  phase range at the wavelength of our excitation source ( $491\ \text{nm}$ ). We also modified the addressing scheme of the SLM. This addressing is digital, which means that the phase levels are created by pulse width modulation. Because of the low addressing rate and limited viscosity of the liquid crystal molecules, the actual phase levels exhibit a certain flicker that is reminiscent from the addressing sequences. Nevertheless, the flicker can be reduced by shortening the pulse sequences and addressing them more often within one frame. Therefore, we switched from the default configuration, designed for 1216 different phase levels, to a custom one with 192 phase levels. This naturally reduces the number of distinguishable phase levels that can be created, which might not suit all applications.

#### ACKNOWLEDGMENTS

We thank Pr. Sheppard and Pr. Heintzmann for many fruitful discussions and encouragement. This work was partially funded by the French Agence Nationale de la Recherche under contract ANR-08-NANO-P053-36.

#### REFERENCES

1. M. Martínez-Corral and G. Saavedra, "The resolution challenge in 3D optical microscopy," *Prog. Opt.* **53**, 1–67 (2009).
2. A. S. van de Nes, J. J. M. Braat, and S. F. Pereira, "High-density optical data storage," *Rep. Prog. Phys.* **69**, 2323–2363 (2006).
3. E. Walker, A. Dvornikov, K. Coblentz, S. Esener, and P. Rentzepis, "Toward terabyte two-photon 3D disk," *Opt. Express* **15**, 12264–12276 (2007).
4. P. C. Chaumet, B. Pouligny, R. Dimova, and N. Sojic, "Optical tweezers in interaction with an apertureless probe," *J. Appl. Phys.* **102**, 024915 (2007).
5. C. Selhuber-Unkel, I. Zins, O. Schubert, C. Sonnichsen, and L. Oddershede, "Quantitative optical trapping of single gold nanorods," *Nano Lett.* **8**, 2998–3003 (2008).
6. M. Dienerowitz, M. Mazilu, and K. Dholakia, "Optical manipulation of nanoparticles: a review," *J. Nanophotonics* **2**, 021875 (2008).
7. C. J. R. Sheppard and Z. S. Hegedus, "Axial behavior of pupil-plane filters," *J. Opt. Soc. Am. A* **5**, 643–647 (1988).
8. M. Martínez-Corral, P. Andrés, C. J. Zapata-Rodríguez, and M. Kowalczyk, "Three-dimensional superresolution by annular binary filters," *Opt. Commun.* **165**, 267–278 (1999).
9. M. Martínez-Corral, M. T. Caballero, E. H. K. Stelzer, and J. Swoger, "Tailoring the axial shape of the point spread function using the Toraldo concept," *Opt. Express* **10**, 98–103 (2002).
10. G. Boyer, "New class of axially apodizing filters for confocal scanning microscopy," *J. Opt. Soc. Am. A* **19**, 584–589 (2002).
11. M. Martínez-Corral, C. Ibanez-Lopez, G. Saavedra, and M. T. Caballero, "Axial gain in resolution in optical sectioning fluorescence microscopy by shaded-ring filters," *Opt. Express* **11**, 1740–1745 (2003).
12. R. Dorn, S. Quabis, and G. Leuchs, "Sharper focus for a radially polarized light beam," *Phys. Rev. Lett.* **91**, 233901 (2003).

13. N. Lindlein, S. Quabis, U. Peschel, and G. Leuchs, "High numerical aperture imaging with different polarization patterns," *Opt. Express* **15**, 5827–5842 (2007).
14. W. Chen and Q. Zhan, "Diffraction limited focusing with controllable arbitrary three-dimensional polarization," *J. Opt.* **12**, 045707 (2010).
15. B. J. Davis, W. C. Karl, A. K. Swan, M. S. Unlu, and B. B. Goldberg, "Capabilities and limitations of pupil-plane filters for superresolution and image enhancement," *Opt. Express* **12**, 4150–4156 (2004).
16. L. Melton, "Imaging: the big picture," *Nature* **437**, 775–779 (2005).
17. S. W. Hell, "Microscopy and its focal switch," *Nat. Methods* **6**, 24–32 (2009).
18. S. W. Hell and E. Stelzer, "Properties of a 4Pi confocal fluorescence microscope," *J. Opt. Soc. Am. A* **9**, 2159–2166 (1992).
19. M. Nagorni and S. W. Hell, "Coherent use of opposing lenses for axial resolution increase in fluorescence microscopy. I. Comparative study of concepts," *J. Opt. Soc. Am. A* **18**, 36–48 (2001).
20. J. Bewersdorf, R. Schmidt, and S. W. Hell, "Comparison of I5M and 4Pi-microscopy," *J. Microsc.* **222**, 105–117 (2006).
21. H. Gugel, J. Bewersdorf, S. Jakobs, J. Engelhardt, R. Storz, and S. W. Hell, "Cooperative 4Pi excitation and detection yields sevenfold sharper optical sections in live cell microscopy," *Biophys. J.* **87**, 4146–4152 (2004).
22. M. Nagorni and S. W. Hell, "4Pi-confocal microscopy provides three-dimensional images of the microtubule network with 100- to 150 nm resolution," *J. Struct. Biol.* **123**, 236–247 (1998).
23. J. Bewersdorf, B. T. Bennett, and K. L. Knight, "H2AX chromatin structures and their response to DNA damage revealed by 4Pi microscopy," *Proc. Natl. Acad. Sci. USA* **103**, 18137–18142 (2006).
24. E. Mudry, P. C. Chaumet, K. Belkebir, G. Maire, and A. Sentenac, "Mirror-assisted optical diffraction tomography with isotropic resolution," *Opt. Lett.* **35**, 1857–1859 (2010).
25. E. Mudry, E. Le Moal, P. Ferrand, P. C. Chaumet, and A. Sentenac, "Isotropic diffraction-limited focusing using a single objective lens," *Phys. Rev. Lett.* **105**, 203903 (2010).
26. R. Carminati, R. Pierrat, J. de Rosny, and M. Fink, "Theory of the time reversal cavity for electromagnetic fields," *Opt. Lett.* **32**, 3107–3109 (2007).
27. C. J. R. Sheppard and K. J. Larkin, "Effect of numerical aperture on interference fringe spacing interferometry," *Appl. Opt.* **34**, 4731–4734 (1995).
28. C. J. R. Sheppard and P. Torok, "Electromagnetic field in the focal region of an electric dipole wave," *Optik* **104**, 175–177 (1997).
29. J.-J. Greffet and R. Carminati, "Image formation in near-field optics," *Prog. Surf. Sci.* **56**, 133–237 (1997).
30. M. Schrader, M. Kozubek, S. W. Hell, and T. Wilson, "Optical transfer functions of 4Pi confocal microscopes: theory and experiment," *Opt. Lett.* **22**, 436–438 (1997).
31. P. Torok and C. J. R. Sheppard, "The role of pinhole size in high-aperture two and three-photon microscopy," in *Confocal and Two-Photon Microscopy*, A. Diaspro, ed. (Wiley-Liss, 2001).
32. H. J. Matthews, D. K. Hamilton, and C. J. R. Sheppard, "Aberration measurement by confocal interferometry," *J. Mod. Opt.* **36**, 233–250 (1989).
33. M. Lang, T. Muller, J. Engelhardt, and S. W. Hell, "4Pi microscopy of type A with 1-photon excitation in biological fluorescence imaging," *Opt. Express* **15**, 2459–2467 (2007).